Thickness distribution of sputtered films on curved substrates for adjustable x-ray optics

Nathan Bishop
Julian Walker
Casey T. DeRoo
Tianning Liu
Mohit Tendulkar
Vincenzo Cotroneo
Edward N. Hertz
Vladimir Kradinov
Eric D. Schwartz
Paul B. Reid
Thomas N. Jackson
Susan Trolier-McKinstry

Thickness distribution of sputtered films on curved substrates for adjustable x-ray optics

Nathan Bishop,[a] Julian Walker,[a,*] Casey T. DeRoo,[b] Tianning Liu,[a,c] Mohit Tendulkar,[c] Vincenzo Cotroneo,[d] Edward N. Hertz,[d] Vladimir Kradinov,[d] Eric D. Schwartz,[d] Paul B. Reid,[d] Thomas N. Jackson,[c] and Susan Trolier-McKinstry[a,e]

[a]Pennsylvania State University, Materials Research Institute, Millennium Science Complex, University Park, Pennsylvania, United States
[b]University of Iowa, Department of Physics and Astronomy, Iowa City, Iowa, United States
[c]Pennsylvania State University, Center for Thin Film Devices, Department of Electrical Engineering, University Park, Pennsylvania, United States
[d]Harvard-Smithsonian Center for Astrophysics, Cambridge, Massachusetts, United States
[e]Pennsylvania State University, Materials Science and Engineering Department, University Park, Pennsylvania, United States

Abstract. Piezoelectric adjustable x-ray optics use magnetron sputtered thin film coatings on both sides of a thin curved glass substrate. To produce an optic suitable for a mission requiring high-angular resolution like "Lynx," the integrated stresses (stress × thickness) of films on both sides of the optic must be approximately equal. Thus, understanding how sputtered film thickness distributions change for convex and concave curved substrates is necessary. To address this, thickness distributions of piezoelectric $Pb_{0.995}(Zr_{0.52}Ti_{0.48})_{0.99}Nb_{0.01}O_3$ films are studied on flat, convex, and concave cylindrical substrates with a 220-mm radius of curvature. A mathematical model of the film thickness distribution is derived based on the geometric properties of the sputter tool and the substrate, and film thicknesses deposited with a commercially available sputtering tool are measured with spectroscopic ellipsometry. Experiment and modeled results for flat and convex curved substrates demonstrate good agreement, with average relative thickness distribution difference of 0.19% and −0.10% respectively, and a higher average difference of 1.4% for concave substrates. The calculated relative thickness distributions are applied to the convex and concave sides of a finite-element analysis (FEA) model of an adjustable x-ray optic prototype. The FEA model shows that, left uncorrected, the relative film thickness variation will yield an optic with an optical performance of 2.6 arc sec half power diameter (HPD) at 1 keV. However, the mirror figure can be corrected to diffraction-limited performance (0.3 arc sec HPD) using the piezoelectric adjusters, suggesting that the tolerances for applying a balanced integrated stress on both sides of a mirror are alleviated for adjustable x-ray optics as compared to traditional static x-ray mirrors. Furthermore, the piezoelectric adjusters will also allow changes in mirror figure over the telescope lifetime due to drift in the stress states of the x-ray surfaces to be corrected on orbit. © *The Authors. Published by SPIE under a Creative Commons Attribution 4.0 Unported License. Distribution or reproduction of this work in whole or in part requires full attribution of the original publication, including its DOI.* [DOI: 10.1117/1 .JATIS.5.2.021005]

Keywords: magnetron sputtering; thickness distribution; adjustable optics; curved substrate; microelectromechanical system.

Paper 18055SS received Jul. 12, 2018; accepted for publication Mar. 7, 2019; published online Mar. 23, 2019.

1 Introduction

Physical vapor deposition encompasses several coating techniques that are used commercially for producing both metal and oxide thin films, including some thin film dielectrics and piezoelectrics.[1–5] For example, sputtered aluminum nitride piezoelectric films are ubiquitous in microelectromechanical system resonators, and sputtered perovskite thin films have been explored for the miniaturization of sensors, actuators, and transducers for applications in public health, defense, transport, and energy.[6–8] Piezoelectric materials have also demonstrated potential for astrophysical observation via adjustable optics; use of sputtered piezoelectric thin film actuators is an enabling technology for adjustable x-ray optics.[9–12]

Adjustable x-ray optics are curved thin shell mirrors, in which the figure can be adjusted postmanufacture by applying a voltage to piezoelectric actuators on the back (convex side) of the mirror.[13–15] When a voltage is applied, a strain is produced by means of the converse piezoelectric effect and this is used to make precise changes to the mirror figure, correcting distortions introduced from processing, mounting, or on-orbit

gravity release.[10,16,17] Our current mirror prototypes consist of thin (0.4 mm) cylindrically curved glass substrates with an ideal radius of curvature (ROC) of 220 mm.[13] A schematic of a curved mirror is shown in Fig. 1(a). The actuators on the back consist of a series of metal (Ti and Pt), piezoelectric $Pb_{0.995}(Zr_{0.52}Ti_{0.48})_{0.99}Nb_{0.01}O_3$ (PZT) layers, and then a top Pt electrode is lithographically patterned to form an array of piezoelectric actuators.[18–22] The front (concave side) is then deposited with Cr and Ir coatings for adhesion and x-ray reflection, respectively.

The curved glass mirrors are thermally slumped onto a mandrel of the desired figure,[23] typically achieving an optical performance of ∼10 arc sec half power diameter (HPD) (single reflection at 1 keV), with a figure peak-to-valley (PV) difference of 2.53 μm before the piezoelectric actuators are added.[13] Current patterns of piezoelectric actuators can conservatively produce a figure change on the order of 10 arc sec, and thus in principle, provide suitable correction for the as-slumped mirrors.[19] Additional sources of distortion must be minimized to keep the mirror figure within the dynamic range of the actuators, and therefore, correctable to the required performance. Identifying, understanding, and minimizing sources of figure distortion associated with the mirror processing is thus necessary.
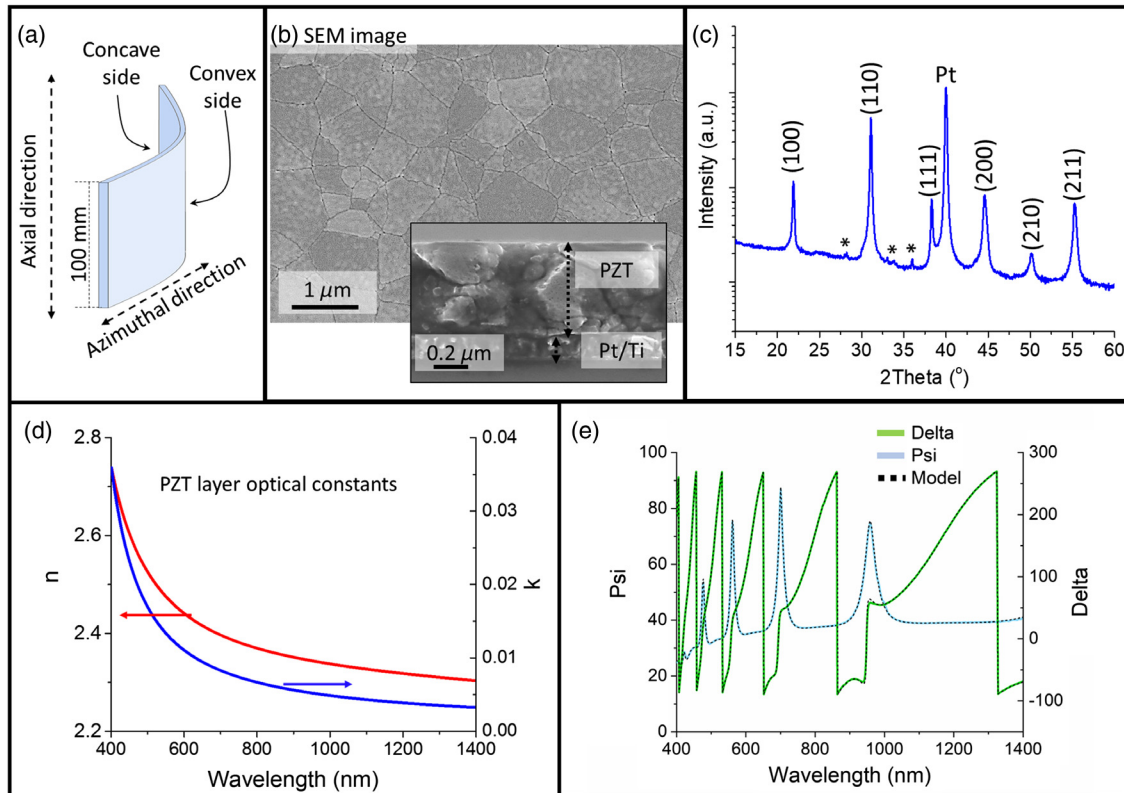
Fig. 1 (a) A schematic of the curved glass mirror where the convex side, concave side, axial, and azimuthal directions are labeled. (b) SEM micrograph of the PZT film surface (inset shows cross section) after crystallization. (c) XRD pattern from crystallized film showing a single-phase perovskite structure; peaks are labeled with pseudocubic notation for the perovskite. In addition, the (111) Pt peak is labeled, and the * symbol indicates instrument-related x-ray peaks. (d) Typical optical constants, refractive index (n), and extinction coefficient (k), determined for the PZT film. (e) Typical ellipsometry spectra Psi (Ψ) and delta (Δ) measured and modeled for the PZT on Pt/glass at an incidence angle of 65°.

The relationship between the change of a substrate's ROC and a film's stress and thickness is expressed by Stoney's formula, for the basic case assuming constant ROC change of a finite, flat, or spherical substrate, deforming within its elastic limits:

$$\sigma_f = \frac{E_s h_s^2}{h_f 6(1 - \vartheta_s)k}, \tag{1}$$

where σ_f is the stress of the deposited film, E_s is the Young's modulus of the substrate, h_s is the thickness of the substrate, k is the change in the ROC, h_f is the thickness of the film, and ϑ_s is the Poisson's ratio of the substrate (or mirror). Stoney's formula indicates that the integrated stress (stress × thickness) of all films deposited on the mirror will influence the figure,[24,25] and as a result, it is important to control both stress and thickness of the films.

Some integrated stress for the piezoelectric layers is unavoidable, as thermal stress develops during the deposition and processing of the thin films due to the thermal expansion mismatch between the films and the glass substrate.[19] The integrated stress of the actuators is in the range of 130 to 190 MPa μm (tensile stress) and depends on the exact film thicknesses and processing temperatures used. One approach for mitigating the effect of the integrated stress is to counterbalance it with an approximately equal integrated stress on the concave side of the mirror. This approach is referred to as stress balancing. In the case of adjustable x-ray optics, Ir coatings up to 400-nm thick are employed to achieve average integrated stresses within 10% of that from the piezoelectric actuator layers. However, this approach requires good integrated stress uniformity between films deposited on the convex and concave sides of the mirror. As the integrated stress depends both on film stress and film thickness, understanding the thickness distribution on both sides of the curved substrate is important for stress balancing.

Radio frequency (RF) and direct current (DC) magnetron sputtering techniques are the preferred deposition methods for fabrication of thin films for adjustable x-ray optics,[15] as the approximate line-of-sight mass trajectory allows films to be deposited on one side of the substrate at a time, while resulting in only limited contamination of the reverse side.[26] Sputtering also allows for the tuning of the metal film stress and microstructure by control of deposition pressure.[26–29] Sputtered film thickness distributions and microstructures are influenced by sputtering parameters such as the deposition chamber geometry,[30–33] substrate rotation,[34–36] configuration of the magnetron,[37–39] and the use of collimators, shadow masks, or differential deposition.[40–43] Controlling thin film thickness uniformity and microstructure becomes more complicated when depositing onto curved substrates as the ROC of the substrate and the angle of the deposition also play a role.[43–48] The use of

shadow masks or differential deposition can modify the film thickness distribution, but requires custom designs for different sputtering configurations and substrates,[49–54] and can be difficult to implement. While specialized magnetron sputtering geometries would be used for adjustable x-ray optics adopted for a flight mission, initial mirror prototypes are made using angled circular off-axis planar magnetrons with rotating substrates. Characterizing the thickness distributions achieved by this sputtering approach is thus important for determining the influence of thickness nonuniformity on the performance of current and future prototypes.

In this work, the thickness distribution of RF magnetron sputtered PZT films on flat, convex, and concave curved glass substrates was investigated. The deposition parameters and sputter geometry were kept constant, and the thickness distribution was measured using spectroscopic ellipsometry for PZT films deposited with a nominal thickness of 0.5 μm. An accompanying mathematical model was also developed for predicting the thickness distribution over the substrate. To determine the influence of film thickness nonuniformity on prototype adjustable x-ray mirrors, we first quantified the thickness distribution inherent to the sputter tool used for deposition, and then determined how substrate curvature influenced the thickness uniformity. The thickness distribution difference between films deposited on the convex and concave side of the curved substrate was then calculated and measured. We then examined the impact of the integrated stress variation, due to nonuniform thickness distributions, on the optical performance of the adjustable mirror. Via finite-element analysis (FEA), we computed the figure error of the mirror due to the variations in integrated stress arising from thickness distributions on the concave and convex sides of the mirror, and assessed whether these errors could be corrected using the piezoelectric actuators. The nonuniform thickness variations from the modeled magnetron sputtering geometry were found to yield an optical performance of 2.5 arc sec HPD (1 keV at a focal length of 8.4 m). This performance is well-outside the requirements of the "Lynx" point spread function (PSF) ($\leq$0.5 arc sec on-axis).[12] However, the introduced figure deformation can be corrected to be diffraction limited to 0.3 arc sec HPD by actuation consistent with currently existing adjustable x-ray optics prototypes. Our results indicate that the tolerances on integrated stress uniformity required for the Lynx mirrors may be alleviated using the piezoelectric actuators of the adjustable x-ray optics, in addition to traditional static approaches.

2 Experimental Method

Samples were prepared with the same experimental parameters used to produce recent adjustable optic prototypes.[13,15,18–21] All films were prepared on 0.4-mm-thick Corning Eagle-XG™ glass substrates. Flat and cylindrical substrates with an ROC of 220 mm were used. Curved glass was slumped by heating the glass to 745°C for 24 h in a box furnace on a silicon mandrel with a sputtered Pt release layer.[23] Glass pieces were laser cut to 101.6×101.6 mm (4×4 in.) dimensions after slumping.

All samples were cleaned prior to film deposition as described elsewhere.[20] Glass substrates were first submerged in a bath of a commercial sulfuric and chromic acid solution (KleanAR, Avantor Perf Mat-Macron Lab) and sonicated for 5 min. The glass was then rinsed in deionized water for 3 min before being submerged in acetone and sonicated for 5 min, then submerged in isopropanol and sonicated for a further

5 min. Substrates were dried with compressed nitrogen gas. Before film deposition, the substrates were treated in an M4L RF gas plasma system (PVA, TePla) for 2 min with 200 W RF power, 150 scm/s oxygen, 50 scm/s helium, and a 550 mTorr chamber pressure.

Metal and oxide films were deposited using a Kurt J. Lesker CMS-18 sputter machine. First, a 0.02-μm-thick Ti adhesion layer, and then a 0.1-μm-thick Pt electrode layer were deposited by DC sputtering at room temperature ($\sim$18 to 22°C) with an Ar chamber pressure of 5 mTorr. A DC bias of 4.4 W/cm^2 was used to achieve growth rates of 1.0 and 2.4 Å/s for Ti and Pt, respectively. PZT coatings were deposited by RF sputtering in a second Kurt J. Lesker CMS-18 vacuum sputter machine. $Pb(Zr_{0.52}Ti_{0.48})_{0.99}Nb_{0.01}O_3$ targets with 5 mol% excess PbO were sputtered at a chamber pressure of 4 mTorr, and an RF power density of 2.0 W/cm^2, to achieve an approximate deposition rate of 0.4 Å/s.[13,19,20] Measured thicknesses ranged from 0.57 to 0.51 μm. The sputter chamber had a sputter up geometry and a throw distance (h) of 136 ± 5 mm. A 3-in. diameter target was offset by $\sim$83 $\pm$ 5 mm (3.25 in.) from the central axis of the substrate (off-axis displacement, l) and was angled at 15 deg toward the center of the chamber. The substrate was rotated continuously during the $\sim$5-h long depositions. During deposition on the convex side of the substrates, the curved glass was mounted using Kapton® at the four corners to hold it to a flat Si carrier wafer. For deposition on the concave side, the curved substrates were also mounted to the carrier wafer using Kapton® at the center of the azimuthal edges of the mirror. In both cases, the Si carrier wafer was placed in a metal ring that fit in the fixtures used to load the sample in and out of the sputter tool through the load lock. (It is noted that this tool is not optimized for depositions on curved substrates). Following deposition, the films were crystallized in a box furnace at 550°C for 18 h with a heating and cooling rate of 10°C/min.

Structural characterization of films was performed by an x-ray diffraction (XRD) lab source diffractometer (PANalytical Empyrean). Scanning electron microscopy was performed with a Leo 1530 field emission scanning electron microscopy. Surface topography measurements were performed with an atomic force microscopy (AFM) (Asylum) in contact tapping mode. For thickness measurement, a spectroscopic ellipsometer (J.A. Woollam) was used with CompleteEASE® software package for fitting of Psi (Ψ) and delta (Δ) spectra measured and modeled as a function of wavelength (λ) from 400 to 1400 nm for three incidence angles (55 deg, 65 deg, and 75 deg). The Pt bottom electrode was treated as completely reflective and was fitted with a B-spline function.[55,56] A Bruggeman effective medium approximation (EMA)-coupled interface layer was used between the Pt substrate and the PZT to account for interface roughness. The PZT refractive index (n) and extinction coefficient (k) were first estimated using a B-spline function for the PZT before these constants were used as starting values with a Tauc–Lorentz oscillator for further refinement of the fit.[57–60] A second EMA-coupled layer was used at the PZT surface with both void (air) and PZT, to account for the surface roughness. For calculation of relative thickness values, all fit parameters other than the PZT film thickness were held constant during the fitting process, to ensure a consistent optical model was applied. For the mathematical modeling of the relative thickness distribution, the software package Wolfram Mathematica® was used.
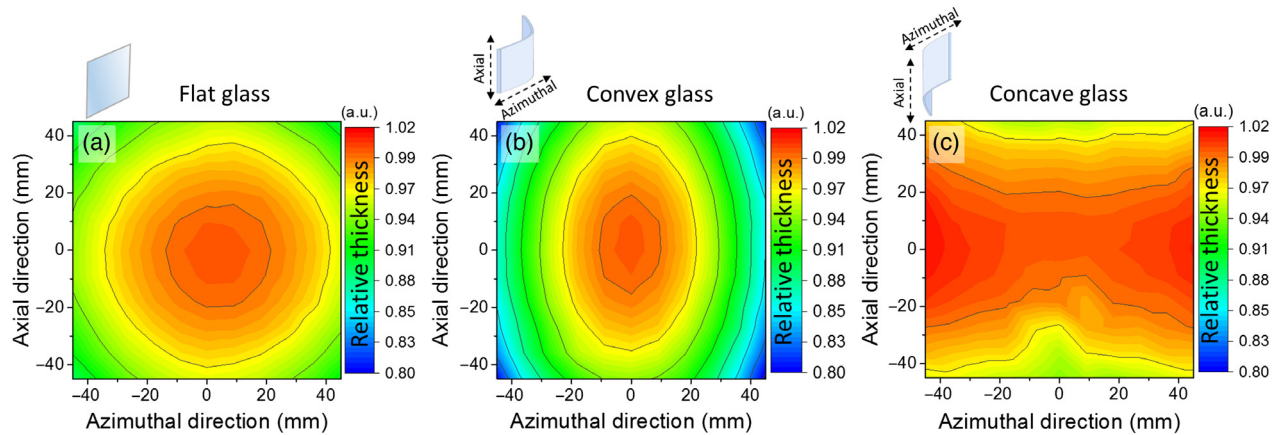
Fig. 2 Relative thickness distribution maps determined by ellipsometry for films on (a) flat, (b) convex, and (c) concave curved glass substrates.

3 Results

3.1 *Measured Film Thickness Distributions*

Both the optical properties and the piezoelectric response of PZT films depend explicitly on the crystal structure and microstructure, including the potential presence of second phases.[6,55] Thus, films were characterized to assess the structure and microstructure prior to ellipsometry measurements. The microstructure exhibited irregular grains with average grain sizes of 375 ± 75 nm to one standard deviation (1σ) and little to no secondary phase, as observed with SEM [Fig. 1(b)]. The structure determined by XRD was a pseudocubic perovskite, consistent with the literature for films near the morphotropic phase boundary [Fig. 1(c)].[55] AFM was used to measure the surface roughness of the films; it was confirmed that the roughness was consistent across the surface area with a root mean square (RMS) roughness of 4.6 nm, and PV surface roughness of 30 nm. This confirmation of structure, phase, and microstructure homogeneity meant that changes in the optical response of the films, measured with spectroscopic ellipsometry as a function of position on the substrate, could be unambiguously interpreted as arising from variations in the film's thickness.

Spectroscopic ellipsometry was used to nondestructively determine the thickness of PZT films as a function of position across each substrate. Measurements were taken in an 11×11 matrix (total of 121 points) across the films. The films exhibited refractive indices (n) values of $\sim$2.4 (at $\lambda \sim 630$ nm) [Fig. 1(d)] and were in good agreement with the literature: 2.6 to 2.3 between 400 and 800 nm.[55,61–63] To determine the film thickness as a function of position, an optical model was fitted to the Ψ and Δ spectra collected from the center of the substrate with typical fit mean square error of 13.36 ± 0.72 [Fig. 1(e)]. Once a good fit was achieved, optical constants and oscillator fit parameters were fixed so that the film thickness parameter could be refined to fit the Ψ and Δ spectra from the other points on the sample.

The measured film thickness values were normalized to the center of each substrate and plotted as a function of position to create relative thickness distribution maps (Fig. 2). For the flat glass substrate, the thickness decreased radially [Fig. 2(a)]. At the corners of the substrate, where the distance from the center was $\sim$70 mm, the relative film thickness was 0.88, whereas at the midpoint of each edge, the relative thickness was 0.95.

For the curved substrate on the convex side, the film thickness distribution was elliptical with a maximum thickness at the center and a minimum thickness of 0.79 at the corners [Fig. 2(b)]. The thickness decrease was greatest in the azimuthal direction with the relative thickness of 0.94 and 0.87 at the midpoint of the edges parallel to the axial and azimuthal directions, respectively.

On the concave side, the film thickness distribution pattern was hyperbolic, with asymptotes passing diagonally through the substrate [Fig. 2(c)]. The relative thickness minimum was 0.94 at the midpoint of the edges parallel to the azimuthal direction, and a maximum of 1.02 at the midpoint of the edges parallel to the axial direction. Deviations from a perfectly symmetrical distribution pattern, seen predominantly in the lower middle region of the distribution map, were most likely related to fluctuations in the film quality caused by mechanical damage and/or contamination of the substrate prior to deposition.

3.2 *Modeled Film Thickness Distribution*

3.2.1 *Geometric film thickness model for flat substrates*

A mathematical model considering the geometry of the sputter tool was developed to predict the thickness distribution of films, similarly as presented in earlier literature.[30–33,38,42,43] To determine the thickness distribution inherent to the sputter tool geometry, the flat substrate case was considered first. Sputtering parameters such as temperature, power, target chemistry, chamber pressure, and gas species were kept consistent throughout the study and were not considered in the model. Figure 3(a) provides a schematic of the sputter chamber, with labels of the geometric factors that were utilized in the model. The three critical dimensions considered were the vertical throw distance (h), the off-axis displacement (l), and the target angle (Ω). The magnetron sputtering tool modeled (Kurt J. Lesker CMS-18) was a commercially available system, and the key dimensions were typical of systems used for small scale or research-based sputtering. The ejected species mass flux was treated as continuous for the duration of sputtering time.

The ejection of the chemical species from each area element on the target (dA) was defined using a cosine distribution, with angle (θ) between the normal to the target surface and the trajectory of ejected species.[30,32] The magnetic field of the magnetron improves deposition rates by increasing the plasma density
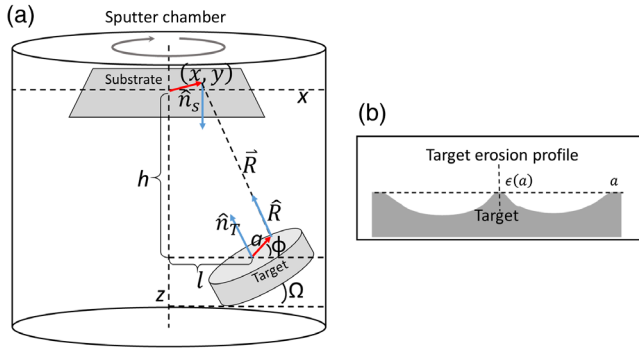
Fig. 3 A schematic of (a) the sputter chamber geometry where the circular gray arrow indicates that the substrate is rotating during deposition and (b) target erosion profile.

near to the target, but results in nonuniform ejection of species as a function of radial position on the target (a), i.e., heterogeneous target erosion.[1] This was apparent from the symmetric radial erosion profile of the target which followed the magnetic field lines [Fig. 3(b)]. The depth of the erosion profile was proportional to the target species ejection rate and was treated in the model by including an erosion function $\epsilon(a)$.[30,32,38,64] The erosion function was approximated as a half sine wave [Eq. (2)], consistent with typical "race track" erosion profiles observed in the literature[38]

$$\epsilon(a) \cong \sin\left(\frac{a\pi}{R_T}\right), \quad (2)$$

where (a) is the radial position on the sputtering target, and R_T is the radius of the target.

A critical consideration for the model was the distance between the target and the substrate. The ejected mass flux decreases proportionally to the inverse square of the distance it travels to the substrate (denoted by the vector $\vec{R}$). This was described via the vertical throw distance (h), the off-axis displacement (l), and the target angle (Ω). A Lambertian distribution term was used for the distribution of mass direction leaving the target at a given point. A cosine term to the power of one was found to achieve the best fit to the experimental thickness distributions measured for both flat and curved substrates. As a result, the mass flux reaching a point on the surface of the substrate (dm_s) is given by

$$dm_s \propto \frac{\epsilon(a)}{|\vec{R}|^2} \cos \theta \, dA, \quad (3)$$

where dA is an element of area on the target from which the atomic species is being ejected, and θ is the angle between the normal of the surface of the target and the direction of species ejection.

It was assumed that mass ejected from the target travels in a straight line until it reaches the substrate surface, i.e., the effects of scatter due to atomic collisions were ignored. The rate of accumulation of mass at a point on a surface (dD, mass per second) is proportional to the cosine of the angle between the direction of the mass trajectory ($\hat{R}$) and the normal of the surface ($\hat{n}_s$). This cosine term was then expressed by the scalar product of two normalized vectors as given in

$$\frac{dD(x,y)}{dt} \propto (-\hat{n}_s \cdot \hat{R})dm_s \propto \frac{\epsilon(a)}{|\vec{R}|^2} \cos \theta (-\hat{n}_s \cdot \hat{R})dA, \quad (4)$$

The cosine term for the angular emission intensity from the target can also be given by the scalar product of two vectors, the vector normal to the surface of the sputtering target ($\hat{n}_T$) and $\hat{R}$. Thus changing Eq. (4) to (5):

$$\frac{dD(x,y)}{dt} \propto \frac{\epsilon(a)}{|\vec{R}|^2} (\hat{n}_T \cdot \hat{R})(-\hat{n}_s \cdot \hat{R}) a \, da \, d\varphi. \quad (5)$$

The area element (dA) could then be given in terms of polar coordinates, where a and φ are the radial and angular coordinates describing a point on the target. From this, the thickness (D) deposited onto a point (x, y) on the surface of the substrate was obtained by integrating Eq. (5) across the area of the target over a given time (t_f):

$$D(x,y) = C \int_0^{t_f} \int_0^{2\pi} \int_0^{R_T} \frac{\epsilon(a)}{|\vec{R}|^2} (\hat{n}_T \cdot \hat{R})(-\hat{n}_s \cdot \hat{R}) a \, da \, d\varphi \, dt. \quad (6)$$

The constant C was used to normalize the thickness to the value 1 at the center of the substrate (i.e., the x, y coordinates 0, 0). Thus, this expression yields a relative thickness distribution across the substrate.

The vectors necessary to complete the calculations $\vec{R}$, $\hat{n}_T$, and $\hat{n}_s$ were defined from the geometry of the sputtering chamber as shown in Eqs. (7)–(9), respectively. We note, however, that Eq. (9) is true only in the case of flat substrates:

$$\vec{R} = \begin{bmatrix} \sqrt{x^2 + y^2} \cos(\omega t + \delta) - l - a \cos \varphi \cos \Omega \\ \sqrt{x^2 + y^2} \sin(\omega t + \delta) - a \sin \varphi \\ a \cos \varphi \cos \Omega - h \end{bmatrix}, \quad (7)$$

where ω is the constant rotation rate of the substrate, and δ is the polar angle of the point (x, y) at the initial time ($t = 0$)

$$\hat{n}_T = (-\sin \Omega)\hat{x} + (-\cos \Omega)\hat{z}, \quad (8)$$

$$\hat{n}_s = \hat{z}. \quad (9)$$

To demonstrate the influence of the geometry of the sputter tool on the relative thickness distribution, thickness distributions were calculated as each parameter was introduced to the model using a 100-mm^2 area for the substrate (Fig. 4). For a circular target positioned directly below the substrate (i.e., $l = 0$), the relative thickness distribution exhibited the expected symmetrical radially pattern, with a maximum at the center and a minimum of 0.69 at the corners [Fig. 4(a)]. When the target was moved off-axis by ∼1.55 in. (i.e., $l = 39$ mm), the thickness profile was likewise displaced, exhibiting a parabolic distribution along the azimuthal direction (i.e., the direction in which the target and substrate axis were still aligned) [Fig. 4(b)]. A near linear distribution was observed in the axial direction (i.e., the direction in which the target was displaced relative to the substrate) with the relative thickness decreasing from 1.56 to 0.54 at the points closest and furthest from the target [Fig. 4(b)]. The introduction of a target angle Ω of 15 deg
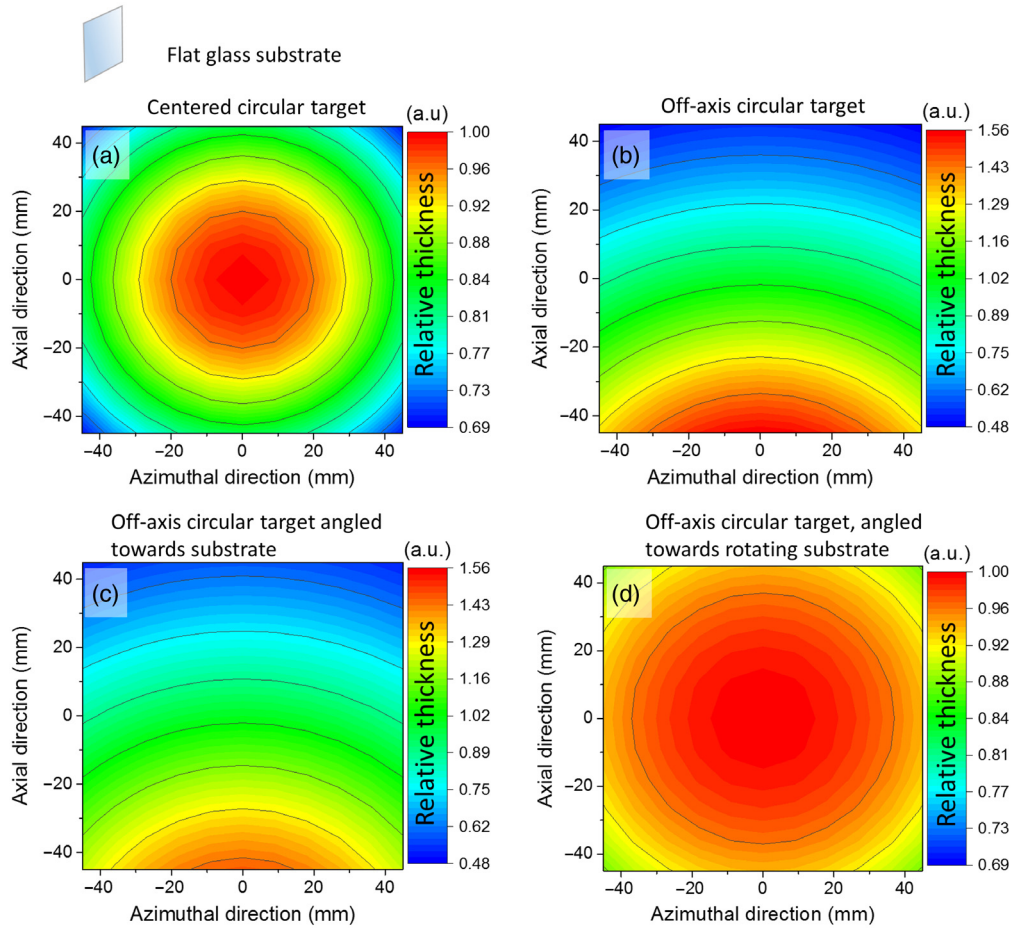
Flat glass substrate

Fig. 4 Modeled relative thickness distributions of a film grown on a 100-mm² substrate for (a) a centered circular 3-in. target, (b) a circular target positioned off axis relative to the center of the substrate, (c) a circular target positioned off axis relative to the substrate and angled toward the substrate at 15 deg and, (d) a circular target positioned off-axis, angled toward the substrate with the substrate rotating continuously during the deposition. Thickness distribution is normalized to the thickness at the center of each substrate. Note different color scales are used for panels (a) and (d) versus panels (b) and (c).

together with the off-axis position introduced almost no change to the thickness distribution along the azimuthal direction, while moderately reducing the thickness distribution in the axial direction, changing the maximum and minimum relative thicknesses to 1.45 and 0.58, respectively [Fig. 4(c)]. Finally, a continuous rotation of the substrate was introduced by making the time-dependent angular rotational frequency $\omega > 0$ [Eq. (8)]; this returned the distribution to a symmetrical radial pattern with the maximum thickness at the center, a minimum relative thickness of 0.89 at the corners and a thickness at the midpoint of each edge of 0.94 [Fig. 4(d)]. The relative thickness distribution seen in Fig. 4(d) corresponds to that of a film deposited on a flat substrate in the sputter tool used for this study.

3.2.2 Geometric film thickness model for curved substrates

The thickness distribution model [Eq. (6)] was modified to account for both convex and concave substrates. The shape of the substrate was incorporated by including the substrate's geometric features into the vector quantities for mass trajectory ($\vec{R}$) and the normal to the substrate surface ($\hat{n}_s$).[65] The vertical throw distance of any point on the substrate $h(x, y)$ was equal to the maximum throw distance h, minus the height of any point on

the substrate $z(x, y)$. Thus, a new expression for $\vec{R}$ was derived. Equation (10) shows the z component for $\vec{R}$, and the x and y components remain the same as given in Eq. (7):

$$\vec{R}_z = a \cos \varphi \cos \Omega - [h - z(x, y)]. \tag{10}$$

Figures 5(a) and 5(b) provides a cross-section schematic of convex and concave substrate geometries, respectively. The associated $z(x, y)$ equations for the convex [Eq. (11)] and concave [Eq. (12)] substrates demonstrate how the substrate ROC, y position, and maximum distance from the center (R_{max}) are used to determine the substrate height at a given point. Given the cylindrical geometry of the substrates (i.e., azimuthal direction curvature and no curvature in the axial direction), only one dimension (y) needs to be considered; however, the z parameter has been kept in (x, y) for application to conical mirror surfaces:

$$z(x, y) = \sqrt{\text{ROC}^2 - y^2} - \sqrt{\text{ROC}^2 - R_{max}^2}, \tag{11}$$

$$z(x, y) = -\sqrt{\text{ROC}^2 - y^2} + \text{ROC}. \tag{12}$$

(a) Convex curved substrate
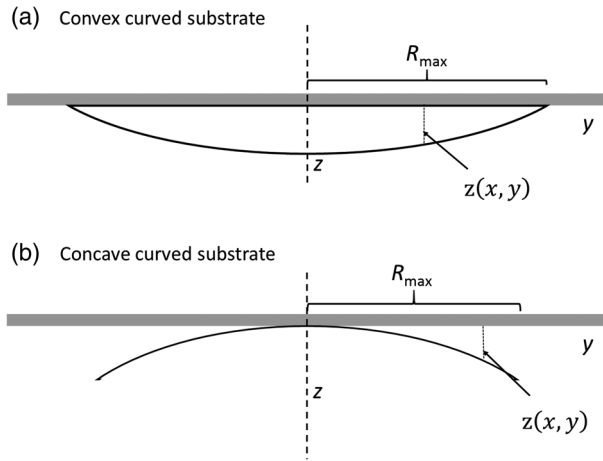
(b) Concave curved substrate

Fig. 5 (a) Convex curved substrate and (b) concave cylindrically curved substrate with equations describing the height (z direction) of an arbitrary point on the substrate as a function of position in the y direction.

The vector normal to the surface of the substrate $\hat{n}_s$ was given by the gradient of the function defining the surface of the substrate $f(x, y, z)$:

$$\vec{n}_s = \vec{\nabla} f(x, y, z) = \left(\frac{y}{\sqrt{\mathrm{ROC}^2 - y^2}} \right) \hat{y} + \hat{z}. \tag{13}$$

While this definition of $\hat{n}_s$ accounted for the substrate curvature, it did not account for the continuous rotation of the substrate during deposition. A rotation operator was thus applied to the vector, rotating it through the angle ωt. A length preserving transformation was used for the rotation operator so that the vector remained normalized

$$\hat{n}_s = \begin{bmatrix} \cos \omega t & -\sin \omega t & 0 \\ \sin \omega t & \cos \omega t & 0 \\ 0 & 0 & 1 \end{bmatrix} \cdot \frac{\vec{\nabla} f(x, y, z)}{|\vec{n}_s|}. \tag{14}$$

The definitions for $z(x, y)$ were used to determine different $\vec{R}$ [Eq. (10)] and $\hat{n}_s$ [Eq. (14)] expressions for the convex and concave cases.

The convex and concave models were then used to estimate their respective relative thickness distributions over a 100-mm^2 surface area. For the convex model, the relative thickness distribution was elliptical with a maximum thickness at the center and a minimum thickness of 0.82 at the corners [Fig. 6(a)]. The thickness decrease was greatest in the azimuthal direction, with relative thicknesses of 0.94 and 0.87 at the midpoint of the edges parallel to the axial and azimuthal directions, respectively.

For the concave model, the thickness distribution pattern was also elliptical with a maximum thickness at the center; however, the axis along which the thickness reduction was greatest rotated by 90 deg [Fig. 6(b)]. The thickness reduced to only 0.98 in the azimuthal direction, whereas the greatest thickness reduction (0.94) occurred in the axial direction. The overall thickness nonuniformity was reduced markedly on a concave substrate relative to a convex substrate.

3.2.3 *Impact of parameter uncertainties in modeled thickness distributions*

The effect of uncertainties in the key geometric parameters of the sputter tool was considered. To evaluate the potential error introduced by an uncertainty in the throw distance, an increase in the throw distance of 5 mm (i.e., $h = 141$ mm) was considered in the model and the thickness distribution was compared to that at nominal h ($h = 136$ mm). In the case of the flat substrate, a PV thickness difference of 0.12% was observed. An uncertainty in the position of the substrate (in the plane perpendicular to the through distance) relative to the nominal position was also considered; we estimate that this uncertainty is no larger than 5 mm given the loading mechanism for the tool. For flat substrates, a 5-mm displacement results in a change in the thickness difference of 2.80% compared to a centered substrate. For a convex substrate, the same displacement in the azimuthal direction results in a change of the thickness difference PV of 3.95%. It was noted that the off-center location of the substrate produced an asymmetric thickness distribution.
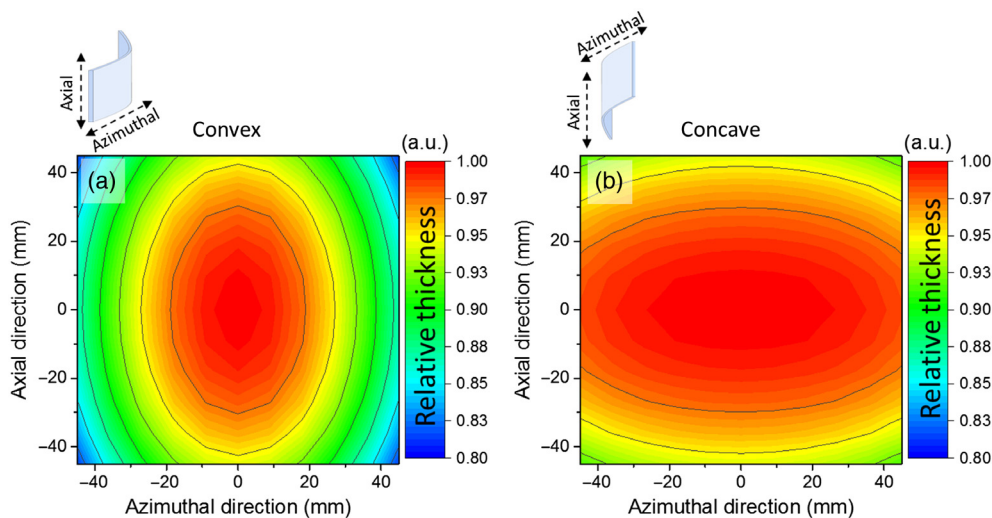

Fig. 6 The modeled thickness distributions for films sputter deposited onto (a) convex and (b) concave curved glass substrates with ROC = 220 mm. Plots show relative thickness as a fraction of the maximum thickness which was located at the center of each substrate.

The impact of uncertainties in the ROC of the substrate was also considered. While the ROC of the mirrors was 220 mm, the mirror figure is nonideal after slumping and varies further with each additional film deposition. As a result, a number of ROCs were considered in the model to determine the magnitude of associated thickness distribution error. Mirrors with a maximum ROC of 227 mm and a minimum ROC of 210 mm were considered; these errors were chosen to represent the range of reasonable uncertainties observed during fabrication of adjustable x-ray optics. The thickness distributions with these ROCs were calculated for convex substrates, in which the total relative thickness variation was higher than that for concave substrates. At an ROC of 227 mm, the PV thickness distribution difference from the nominal distribution was 0.29%, and for a 210-mm ROC it was 0.46%. The effect of nonideal ROCs was thus not considered a significant factor of the relative thickness distributions.

4 Discussion

4.1 Comparing Measured and Modeled Thickness Distributions

The measured and the modeled relative thickness distributions were compared for each of the substrate geometries by considering the standard deviation of the relative thickness and the difference between the measured and modeled values for each

Table 1 Comparison of the modeled and measured relative thickness variation across flat, convex, and concave curved substrates.

	Standard deviation of relative thickness over the total substrate area		Measurement–model relative thickness difference (%)	
	Modeled	Measured	Average	Standard deviation
Flat	0.027	0.027	0.19	0.59
Convex	0.051	0.053	−0.10	1.08
Concave	0.023	0.014	1.45	1.40

case (Table 1). Relative thickness difference maps were plotted for each case (Fig. 7).

The modeled distributions were in excellent agreement with the measured results. For flat and convex substrates, the standard deviations of relative thickness over the substrate area were almost the same, with average relative thickness differences of 0.19% and −0.10% and maximum differences of 1.71% and −1.85%, respectively (Table 1).

According to our model [Fig. 6(b)], concave substrates have the smallest relative thickness variation PV, and therefore, the greatest overall thickness uniformity. However, the average relative thickness difference between the measured and the modeled results was 1.45% with a standard deviation of 1.40% and a maximum of 5.74%, significantly larger than that for flat and convex substrates. The difference map clearly showed an elliptical pattern with the maximum error increase parallel with the azimuthal direction, indicating that the model mostly under estimated the film thickness [Fig. 7(c)].

The model for curved substrates is based on the principle that the substrate ROC affects the thickness distribution by changing the mass flux at the substrate (which is inversely proportional to the square of $\vec{R}$) [Eq. (7), Fig. 5], and the vector normal to the substrate surface ($\vec{n}_s$) [Eqs. (13) and (14)]. There was some spatially correlated error visible in the maps for flat and convex substrates [Fig. 7(a) and 7(b)]. We attribute this to a small (e.g., <1 mm) substrate off-centering from the center of rotation, as indicated by the model's off-center error considerations (see Sec. 3.2.3).

Another assumption made in the model is the erosion profile $\epsilon(a)$, which is estimated using a half sine wave function.[30] The model does not account for the fact that over the lifetime of the target the erosion profile shifts as the magnetic field becomes stronger at the locations where the target thickness is reduced. The plasma density and deposition rates will thus vary as the target erodes, correlating with changes in the film growth rate distribution over the substrate.[32,64,66,67] Moreover, as the target erodes, the surface becomes increasingly less flat, which increases the error of the vector normal to the substrate surface $\hat{n}_T$.[68] The area of the target producing the largest mass flux coincides approximately with the largest error in $\hat{n}_T$, and thus may influence the measurement-model error. However, the target geometry is identical in all depositions, and hence does not explain the observed error occurring only in the concave case.
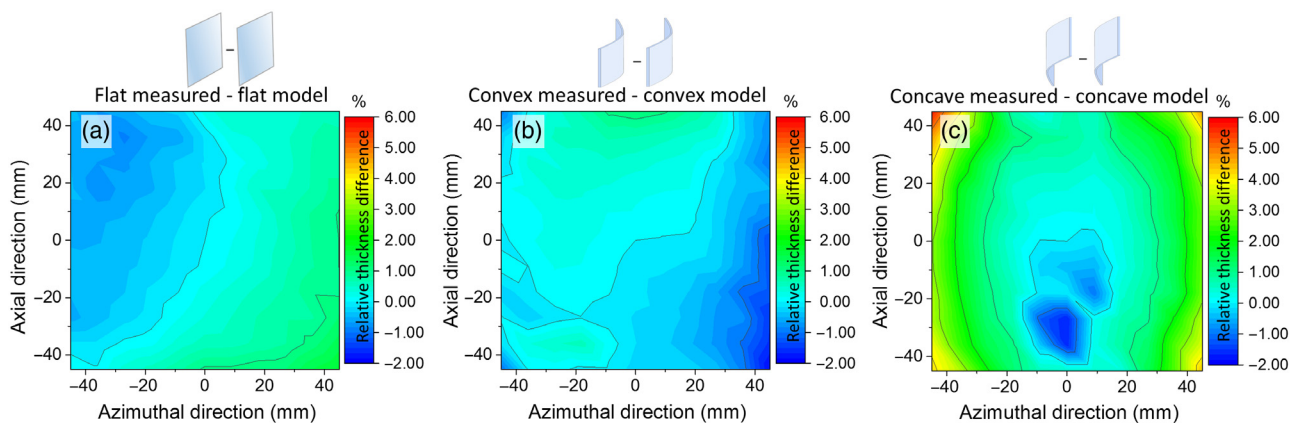

Fig. 7 Relative thickness difference maps showing the modeled relative thickness subtracted from the measured relative thickness for (a) flat, (b) convex, and (c) concave curved substrates. Color scales are the same for all figures.
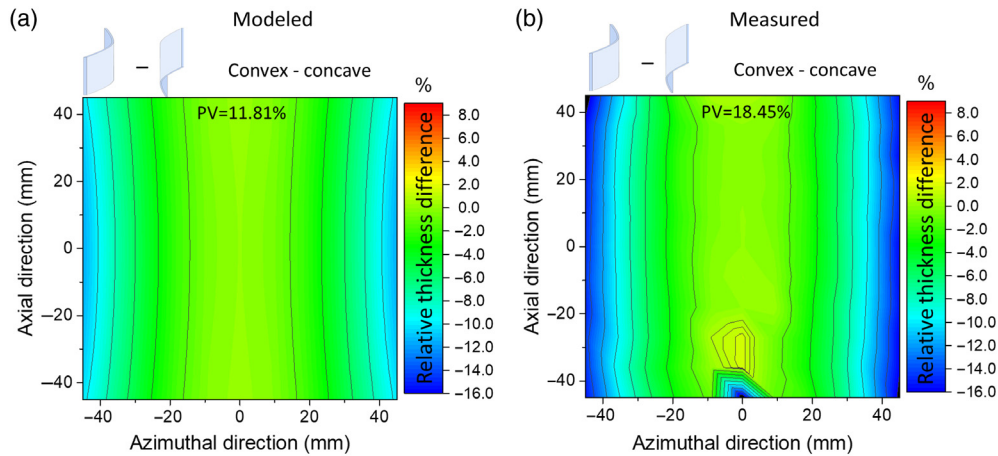
Fig. 8 The effect of substrate curvature on (a) modeled and (b) measured relative thickness distributions, respectively, examined by subtracting the distributions of a convex substrate from a concave substrate. Note that both figures have the same color scale and PV values are given in this figure.

4.2 Net Thickness Nonuniformity for Curved Mirrors

The thickness distribution differences between films deposited on the convex and concave sides of a substrate are critical for adjustable x-ray optics that employ a stress balancing approach, which aims to balance the integrated stress of films deposited on opposite sides of the mirror.[13,19] The difference in the thickness profiles of films deposited on convex and concave sides of the mirror indicates the nonuniformity of the integrated stress that will arise, assuming the stress is homogeneous throughout the films. The relative thickness distribution difference maps were analyzed by subtracting the relative thickness distributions of films on convex substrates from those of concave substrates. Both the modeled and the measured thickness distributions were considered [Figs. 8(a) and 8(b)]. In both cases, the major relative thickness difference occurred in the azimuthal direction, where the maximum difference was −12% for the modeled and −16% for the measured results. The negative sign indicates that in the azimuthal direction the film on the concave side was thicker than the film on the convex side. In the axial direction, the relative thickness difference was significantly less than in the azimuthal direction. Moreover, the measured results show a greater difference than the modeled results, with a maximum variation from the top azimuthal edge of the mirror to the bottom azimuthal edge of <1.5% down the center, and <2.0% down the axial edges.

To maintain high x-ray reflectance, x-ray optics are operated at grazing incidence (grazing angle $\alpha < 2$ deg). This means that the ultimate imaging quality of an x-ray optic is predominantly controlled by axial figure error and is relatively insensitive to azimuthal figure error (by a factor of the sine of the grazing angle).[10,13,14] Thus, the small relative thickness difference between convex and concave films in the axial direction (<2.0%) is advantageous for adjustable x-ray optics.

4.3 Impact of Integrated Stress Nonuniformity on Optical Performance

To quantify the impact of the thickness nonuniformity on the optical performance of the mirror, an FEA model of a prototype adjustable x-ray optic deforming under the integrated stress of thin films deposited on convex and concave sides of the mirror

was constructed. The FEA model assumes a substrate of Corning Eagle-XG™ glass 101.6-mm long with an ROC of 220 mm, a half cone (graze) angle of 0.375 deg, and a thickness of 0.4 mm. Similar FEA models of adjustable x-ray optics have previously been validated with empirical measurements.[13,14]

The resulting narrow aperture (∼0.66 mm) yields a diffracted image size of 0.3 arc sec at 1 keV (1.24 nm wavelength). The effects of aperture diffraction (i.e., the diffraction limit) are included in the calculation of the grazing incidence PSF and cannot be removed from the calculation.

For a telescope such as that proposed for Lynx, two important factors greatly mitigate the impact of diffraction on imaging. First, most of the telescope effective area at 1 keV is provided by mirror segments with much larger graze angles, and therefore, radially much larger entrance apertures (∼95% of the 1-keV effective area is produced at graze angles greater than ∼0.72 deg, with ∼65% of the effective area produced at graze angles >1.4 deg). Second, the adjustable x-ray optics mirror design utilizes 200-mm-long mirror segments, which doubles the radial span of the segment entrance aperture(s). For the full telescope design, the area-weighted diffraction contribution for 1-keV x-rays is 0.045 arc sec RMS diameter. This nonzero contribution to imaging is nearly negligible, impacting the PSF HPD and RMS diameter at the level of 1%. Thus, a 0.3-arc sec diffraction limit quoted in this work is an artifact of the shorter length and shallower graze angle for the prototype mirrors and used for the FEA and are not representative of the effective diffraction limit for Lynx optics. These prototype mirror dimensions are used in our development program in response to fabrication and test facility limitations.

To model the effects of nonuniform film thicknesses, the integrated stress at the center of the mirror on both the concave and convex sides was set to 180 MPa μm, which was the average integrated stress of the PZT layer when deposited on our adjustable x-ray optic prototypes.[13] The integrated stress was then allowed to vary proportionally to the relative thickness distribution differences as predicted by the geometric sputtering model developed in Sec. 3.2.2 and shown in Fig. 6. With this integrated stress input, the FEA model was then solved for the radial displacement, axial slope, and azimuthal slope errors over the mirror surface. Using a Fresnel-based numerical method,[69] the PSF of the optic was calculated using these FEA
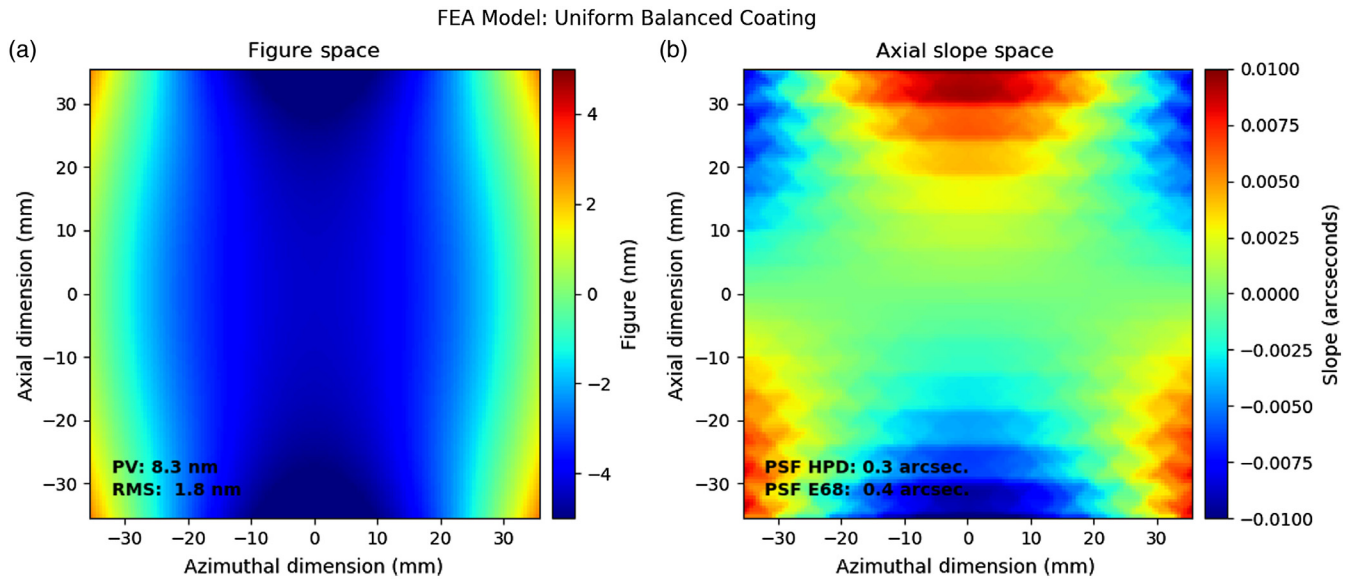
Fig. 9 (a) Figure and (b) axial slope maps of the deformation caused by the application of uniform, stress balanced thin film coatings to the concave and convex sides of the optic. Shown here is the interior (71.6 mm × 71.6 mm) area of the mirror. The integrated stress of the coating is 180 MPa μm. The single reflection performance of this optic at 1 keV is 0.3 arc sec HPD, which is consistent with the diffraction limit of an x-ray optic in this geometry.

outputs. A perimeter of 15 mm is excluded from the PSF calculation in relation to current fabrication development. Thus the mirror's performance was assessed over the interior area (71.6 mm × 71.6 mm), consistent with the PSF calculations previously performed for prototype adjustable x-ray optics.[13] The PSF calculation assumes a single reflection of 1-keV x-rays from a primary Wolter-I mirror segment with a radius of 220 mm and a focal length of 8.4 m, yielding a graze angle of 0.375 deg. In order to quantify x-ray performance from the calculated PSF, both the HPD and the 68% encircled energy diameter (E68) of the calculated PSF are reported.

First, as a point of reference, the FEA model was used to predict the deformation due to films of uniform thickness applied on both the concave and convex sides of the mirror, i.e., the case in which the concave and convex sides of the mirror are subject to the same uniform integrated stress. There is a small change in this figure of the optic in this case. Figure 9(a) shows the relative change in the mirror's figure from the nominal optical prescription, where the color bar indicates the total out-of-plane deviation from this ideal figure in nanometers. Figure 9(b) depicts the gradient of the relative figure changes taken along the optical axis of the mirror and thus represents the axial slope error of the mirror under these conditions. The axial slope error is not zero, since the finite thickness of the glass means that the ROC on the convex side is not identical to the ROC on the concave side. However, the induced slope error observed is negligible, resulting in a diffraction-limited optic (HPD of 0.3") as would be expected in the case of equivalent stresses applied on the convex and concave surfaces.

The apparent pixelation of the slope map [Fig. 9(b)] is an artifact of the finite-element modeling process, which used both solid and shell elements in the interest of computational efficiency. Using much more computationally intense, fully solid element models on a limited number of test cases, does not alter the conclusions, changing numeric results (RMS slope, PSF size) only at the level of <1% in the axial direction and

a few percent in the less significant azimuthal direction. This explanation is applicable to all the axial slope space figures.

Next, the FEA model was used to predict the deformation due to the modeled thickness variations on the concave and convex sides of the mirror, which are shown in Fig. 6. The resulting change in the figure space and axial slope space introduced is shown in Fig. 10. Despite a maximum relative thickness difference between concave and convex films in the axial direction of <2.0%, the resulting figure of the mirror has a PV value of 724 nm [Fig. 10(a)], and the optical performance has degraded to 2.5 arc sec HPD. This performance is outside the requirements for Lynx if left uncompensated. However, the piezoelectric actuators of the adjustable optic can be employed to correct for the deformation induced by the nonuniform coating thickness.

Using the FEA model of the mirror, a correction to the mirror to optimize x-ray performance was simulated. This correction employs an adjuster pattern of 288 cells measuring 5 mm axially by 5 mm azimuthally. It was assumed that the strain exerted is comparable to the PZT strain exerted by cells for an existing adjustable x-ray optic. A least-squares correction algorithm, which optimizes optical performance over the interior 71.6 mm × 71.6 mm area of the optic, is employed to calculate the voltages to apply to the piezoelectric cells.[13,19] The figure of merit for the optimization is a weighted RMS slope, in which the RMS axial slope is added to the RMS azimuthal slope weighted by a factor of the sine of the grazing angle, since slope errors in the axial direction dominate the optical performance of a mirror segment. The optical performance optimization is also constrained to keep the actuation voltage of any individual piezoelectric actuator cell under 10 V.[13] The optimized mirror figure is shown in Fig. 11, and results in a figure with a PV of 418 nm, arising primarily from figure displacement which runs in the azimuthal direction are relatively constant in the axial direction [Fig. 11(a)]. In terms of axial slope, however, the mirror is free from major errors [Fig. 11(b)]. Thus, the correction results in
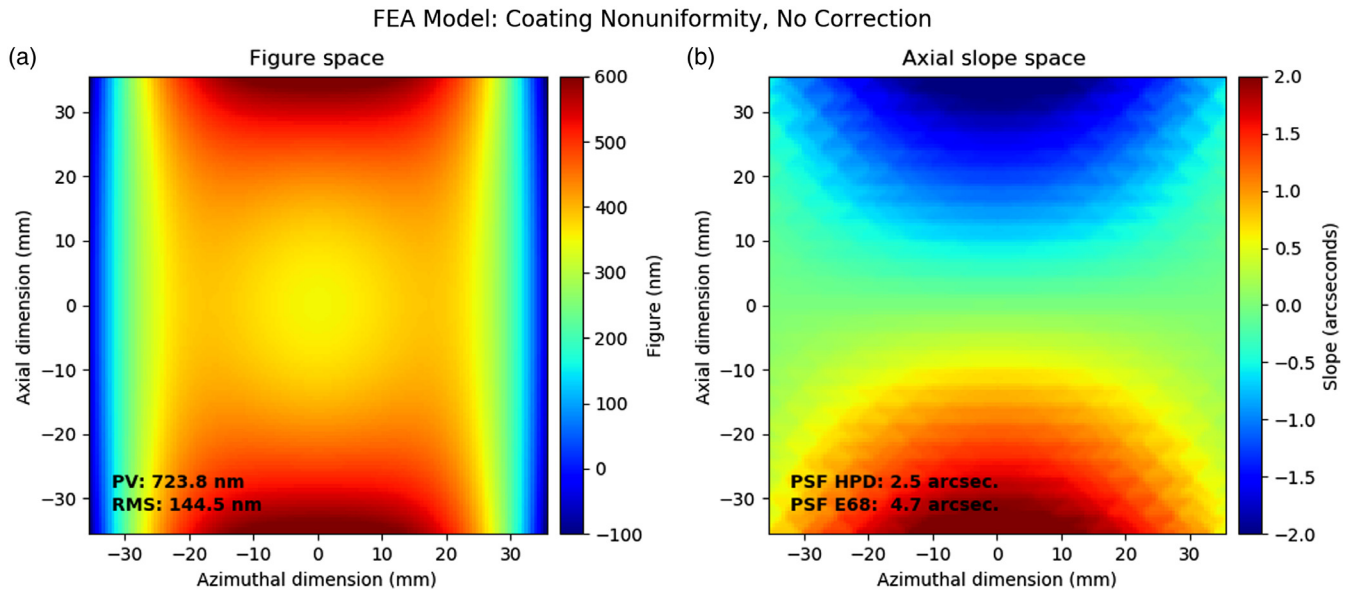
FEA Model: Coating Nonuniformity, No Correction

Fig. 10 (a) Figure and (b) axial slope maps of the deformation caused by nonuniform coating on the concave and convex sides of the optic as calculated using the model presented in Sec. 3. The integrated stress of the coating at the central point is 180 MPa μm on either side, and the integrated stress varies on either side according to the thickness variation presented in Fig. 6. The single-reflection performance of this mirror at 1 keV is 2.6 arc sec HPD.
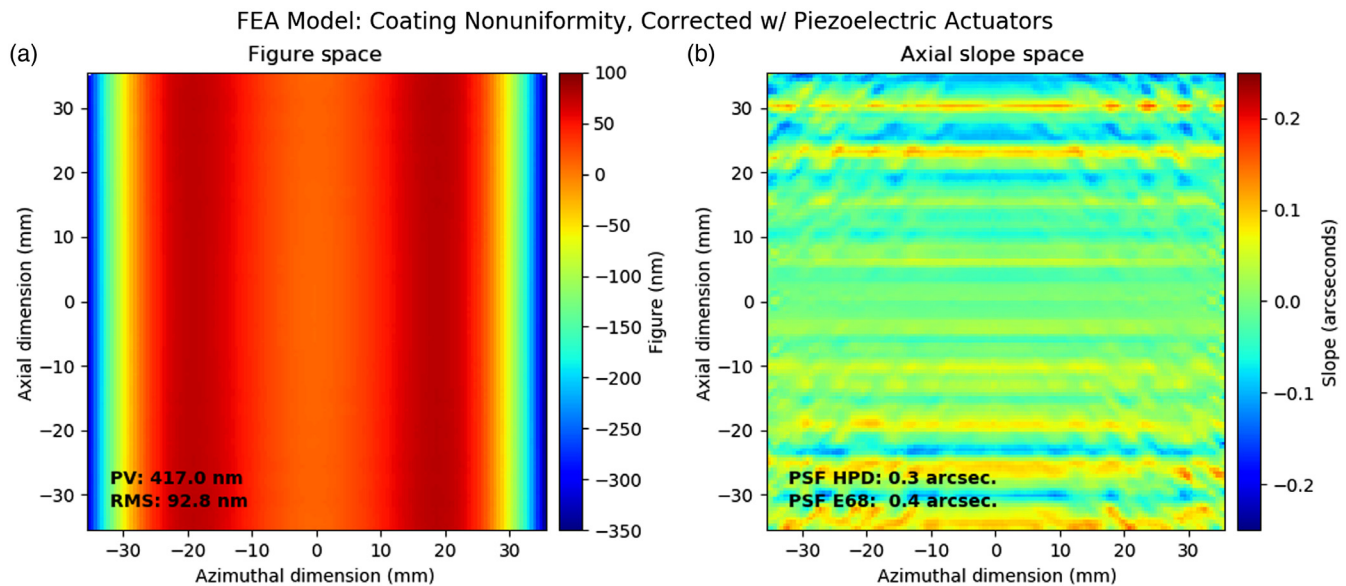
FEA Model: Coating Nonuniformity, Corrected w/ Piezoelectric Actuators

Fig. 11 (a) Figure and (b) axial slope maps of the adjustable x-ray optic following correction. The initial deformation is assumed to be that presented in Fig. 10. A least-squares routine is then employed to calculate the optimal voltage to apply to each piezoelectric cell. The discontinuities visible in the axial slope space map represent the edge of a row of cells. The single-reflection performance of this corrected mirror figure at 1 keV is 0.3 arc sec HPD, consistent with the diffraction limit for an optic in this geometry.

a diffraction-limited optical performance of 0.3 arc sec HPD, similar to the uniform, stress balanced case presented in Fig. 9. Thus, thickness nonuniformity difference of the coatings deposition on convex and concave sides of the mirror results in a deformation that can be theoretically corrected by the piezoelectric actuators of the adjustable x-ray optics.

4.4 Methods for Reducing Thickness Nonuniformity

A sputter tool with an angled circular off-axis planar magnetron is designed for depositions on flat substrates and is not ideal for depositing coatings of high-thickness uniformity on large (>100 mm^2) convex and concave substrates. However, the small difference in low-axial thickness distribution between

convex and concave coatings on the curved substrate is a promising result for prototype adjustable x-ray optics.

The developed thickness distribution model indicates pathways toward reducing the thickness nonuniformity. For example, increasing the throw distance (h) reduces the influence that the change in substrate height $z(x, y)$ has on the thickness distribution, thus reducing the thickness nonuniformity arising due to the substrate curvature. However, sputtering rates and efficiency also reduce as the throw distance is increased [see Eq. (3)]. One method for maintaining high-sputtering rates while achieving high-thickness uniformity can be achieved in planar magnetron systems by utilizing correction masks that effectively cloak the ejected mass after leaving the target to control what reaches the substrate.[49–51,70] Another approach is to use two or more magnetron targets of the same composition and position the rotating substrate equidistant between them.[71] However, such designs do not improve sputtering efficiency and require custom designs for each substrate with a different ROC.

The parameters $\hat{R}$, $\hat{n}_T$, and $\hat{n}_s$ play an important role on the thickness uniformity of films deposited on curved substrates [see Eq. (6)], particularly the angular distribution of $\hat{R}$, as discussed in Sec. 4.1. As a result, magnetron designs which restrict the angular distribution of depositing mass flux together with specific masking designs may be an effective means of improving thickness uniformity. This may be achieved using sputtering tools with collimators,[40–42] high substrate-target angles (i.e., 90 deg)[68] or hollow cathode magnetrons. Collimators placed above the sputtering target can restrict the depositing mass flux to normal incidence angles of ± 5 deg, which might be expected to reduce the thickness nonuniformity on curved substrates. However, collimators do not necessarily overcome thickness variations resulting from target erosion profiles.[41] 90-deg off-axis sputter configurations effectively remove the erosion profile's influence from the spatial distribution of mass flux, but often at the expense of sputtering efficiency.[68] Hollow circular magnetrons utilizing unbalanced magnetic fields and a low-energy ion flux; on the other hand, have demonstrated thickness distributions with little dependence on substrate ROC.[39] Substrates with a 200-mm ROC recorded <0.15% variation of thickness across a 120-mm diameter area, and some studies have already indicated the feasibility of up scaling hollow magnetron sputter configurations for wider use.[72]

For sputter deposition on large substrates or on an industrial scale, moving bar or plate planar magnetrons are often used and are likely a feasible approach for adjustable x-ray optics.[73] Long axial planar magnetrons were used to coat the interior (x-ray reflective side) of the optics for the Chandra x-ray Observatory.[74] For adjustable x-ray optic mirrors, which may have sizes up to 400 mm^2, multiple mirrors could be coated simultaneously, using two or more long-plate axial magnetrons, together with specially designed collimators or shields and a method of rotating the shell past the magnetrons. However, the specific design of the sputter tool would need to vary according to ROC of the mirrors. Alternatively, a directionally controlled mass flux from a long-plate magnetron with a collimator could be coupled with a side-to-side substrate movement parallel to the azimuthal direction. To reduce the nonuniformity in the azimuthal direction, the speed of the substrate movement could be changed as a function of ROC to control the total mass flux at the substrate surface. Such a method may provide a desired higher throughput of mirrors and also allow for multiple mirrors to be coated simultaneously.

It should also be acknowledged that in addition to controlling thickness uniformity, spatially controlled stress of deposited thin films may be a useful approach for stress balancing of adjustable x-ray optics.[75,76] However, for adjustable x-ray optics, this approach is only possible for the Cr/Ir coating on the concave side of the mirrors. This is because the films deposited on the convex side of the mirror require thermal excursions to crystallize the PZT after deposition, and thus the final stress is governed predominantly by the thermal expansion coefficient mismatch between the films and the substrate, rather than the deposition parameters.

5 Conclusions

The thickness distribution of a PZT thin film deposited by RF magnetron sputtering using an off axis angled circular planar magnetron with a rotating substrate was mapped on 101.6 mm^2 flat, convex, and concave curved substrates (ROC of 220 mm) using spectroscopic ellipsometry. For the specific geometry of the sputter tool used, flat substrates exhibited a radial thickness distribution, with thickness decreasing as a function of increasing distance from the center and a thickness of 0.94 at the midpoint of the substrate edge. The convex substrate exhibited an elliptical thickness reduction, with relative thickness at the edges in the axial and azimuthal directions of 0.94 and 0.87. The concave substrate exhibited a relative thickness variation of 1.02 in the azimuthal direction and 0.94 in the axial direction. The mathematical model developed showed excellent agreement with measured results for flat and concave substrates with an average measurement-model difference of 0.19% and −0.10%, respectively. A larger average difference of 1.45% was observed for concave substrates. The key geometric parameters influencing the thickness distribution as a function of substrate curvature were the distance of a given point on the substrate surface from the target (mass trajectory vector) and the angle between the mass trajectory and the normal to the substrate surface at a given point. The relative thickness distributions differences of films on convex and concave substrates provided a benchmark value for the expected change in integrated stress across films on both sides of an x-ray mirror due to thickness nonuniformity. This analysis showed that predicted relative thickness differences in the axial direction were between 0.17% and −1.5%, and as high has −16% in the azimuthal direction. This relative thickness difference results in a variation in the integrated stress over the convex and concave sides of the optic. Employing an FEA model, we show this variation in integrated stress would result in an optical performance of 2.5 arc sec HPD at 1 keV. However, the actuators of an adjustable x-ray optic can correct this introduced figure error, resulting in a diffraction-limited (0.3 arc sec HPD) optic that is consistent with Lynx requirements. Previous studies indicate that shadow or correction masking or use of circular hollow magnetrons may be effective methods for reducing thickness variations on curved substrates. However, the ability of adjustable x-ray optics to correct for deformations may ease tolerances on the variation of integrated stress, and therefore, ease requirements on the coating process for the Lynx mirrors.

References

1. K. Wasa, *Handbook of Sputter Deposition Technology, Fundamentals and Applications of Functional Thin Films, Nanomaterials and MEMS*, 2nd ed., Elsevier Science, Waltham, Massachusetts (2012).

2. M. Ohring, *Materials Science of Thin Films*, 2nd ed., Academic Press, London (2002).

3. P. F. Carcia et al., "Transparent ZnO thin-film transistors fabricated by RF magnetron sputtering," *Appl. Phys. Lett.* **82**(7), 1117–1119 (2003).

4. K. Sreenivas, M. Sayer, and P. Garrett, "Properties of dc magnetron-sputtered PZT thin films," *Thin Solid Films* **172**, 251–267 (1989).

5. S. B. Krupanidhi et al., "RF planar magnetron sputtering and characterization of ferroelectric Pb(Zr, Ti)O$_3$," *J. Appl. Phys.* **54**, 6601–6609 (1989).

6. P. Muralt, R. G. Polcawich, and S. Trolier-McKinstry, "Piezoelectric thin films for sensors, actuators, and energy harvesting," *MRS Bull.* **34**(9), 658–664 (2009).

7. P. Muralt, "Recent progress in materials issues for piezoelectric MEMS," *J. Am. Ceram. Soc.* **91**(5), 1385–1396 (2008).

8. S. Trolier-McKinstry and P. Muralt, "Thin film piezoelectrics for MEMS," *J. Electroceram.* **12**(1–2), 7–17 (2004).

9. J. Fanson, "On the use of electrostrictive actuators in recovering the optical performance of the hubble space telescope," *MRS Proc.* **360**, 109–118 (1994).

10. A. Vikhlinin et al., "SMART-X, square meter, arcsecond resolution x-ray telescope," *Proc. SPIE* **8443**, 844316 (2012).

11. D. A. Schwartz et al., "Technology requirements for a square meter, arcsecond resolution telescope for x-rays: the SMART-X mission," *Proc. SPIE* **9208**, 920806 (2014).

12. J. A. A. Gaskin et al., "Lynx Mission concept status," *Proc. SPIE* **10397**, 103970S (2017).

13. C. T. DeRoo et al., "Deterministic figure correction of piezoelectrically adjustable slumped glass optics," *Proc. SPIE* **10399**, 103991M (2017).

14. R. Allured et al., "Improved control and characterization of adjustable x-ray optics," *Proc. SPIE* **9603**, 96031M (2015).

15. R. H. T. Wilke et al., "Fabrication of adjustable cylindrical mirror segments for the SMART-X telescope," *IEEE Trans. Ultrason. Ferroelectr. Freq. Control* **61**(8), 1386–1392 (2014).

16. B. Jaffe, W. R. Cook, and H. Jaffe, *Piezoelectric Ceramics*, Academic Press, London and New York (1971).

17. N. N. Rogacheva, *The Theory of Piezoelectric Shells and Plates*, Taylor & Francis Group, CRC Press, London (1994).

18. R. H. T. Wilke et al., "Sputter deposition of PZT piezoelectric films on thin glass substrates for adjustable x-ray optics," *Appl. Opt.* **52**(14), 3412–3419 (2013).

19. J. Walker et al., "Design and fabrication of prototype adjustable x-ray mirrors," *Opt. Express* **26**, 27757–27772 (2018).

20. J. Walker et al., "Design and fabrication of adjustable x-ray optics using piezoelectric thin films," *Proc. SPIE* **10399**, 103991K (2017).

21. R. L. Johnson-Wilke et al., "Improving yield of PZT piezoelectric devices on glass substrates," *Proc. SPIE* **8503**, 85030A (2012).

22. M. Wallace, "Performance of PZT based MEMS devices with integrated ZnO Electronics," PhD dissertation, Pennsylvania State University, Department of Materials Science and Engineering (2016).

23. V. Cotroneo et al., "Thermal forming of glass substrates for adjustable optics," *Proc. SPIE* **10399**, 103990Y (2017).

24. G. G. Stoney, "The tension of metallic films deposited by electrolysis," *Proc. R. Soc. London Ser. A* **82**, 172–175 (1909).

25. G. C. A. M. Janssen et al., "Celebrating the 100th anniversary of the Stoney equation for film stress: developments from polycrystalline steel strips to single crystal silicon wafers," *Thin Solid Films* **517**, 1858–1867 (2009).

26. J. A. Thornton, "Influence of apparatus geometry and deposition conditions on the structure and topography of thick sputtered coatings," *J. Vac. Sci. Technol.* **11**, 666–670 (1974).

27. J. A. Thornton, "The microstructure of sputter-deposited coatings," *J. Vac. Sci. Technol. A* **4**, 3059–3065 (1986).

28. D. W. Hoffman and J. A. Thornton, "Effects of substrate orientation and rotation on internal stresses in sputtered metal films," *J. Vac. Sci. Technol.* **16**, 134–137 (1979).

29. J. C. Helmer and C. E. Wickersham, "Pressure effects in planar magnetron sputter deposition," *J. Vac. Sci. Technol.* **4**, 408–412 (1984).

30. S. Swann, S. A. Collett, and I. R. Scarlett, "Film thickness distribution control with off-axis circular magnetron sources onto rotating substrate holders: comparison of computer simulation with practical results," *J. Vac. Sci. Technol.* **8**, 1299–1303 (1990).

31. R. J. Gnaedinger, Jr., "Some calculations of the thickness distribution of films deposited from large area sputtering sources," *J Vac. Sci. Technol.* **6**, 355–362 (1969).

32. E. J. McInerney, *Computational Explorations in Magnetron Sputtering*, Basic Numerics Press, San Jose, California (2014).

33. X. S. Du et al., "Quantitative evaluation of film thickness uniformity: Application of off-axis magnetron source onto a rotating substrate," *J. Vac. Sci. Technol. A* **25**, 215–220 (2007).

34. M. Gross, S. Dligatch, and A. Chtanov, "Optimization of coating uniformity in an ion beam sputtering system using a modified planetary rotation method," *Appl. Opt.*, **50**(9), C316–C320 (2011).

35. V. K. Jayaraman et al., "Importance of substrate rotation speed on the growth of homogeneous ZnO thin films by reactive sputtering," *Mater. Lett.* **169**, 1–4 (2016).

36. N. Panich and Y. Sun, "Effect of substrate rotation on structure, hardness and adhesion of magnetron sputtered TiB2 coatings on high speed steel," *Thin Solid Films* **500**, 190–196 (2006).

37. J. A. Thornton, "High rate sputtering techniques," *Thin Solid Films*, **80**, 1–11 (1981)

38. S. Hong et al., "A simulation model for thickness profile of the film deposited using planar circular type magnetron sputtering sources," *J. Vac. Sci. Technol. A* **14**, 2721–2727 (1996).

39. D. Glocker et al., *System for Sputtering Uniform Optical Coatings on Flat and Curved Surfaces Without Masks*, Kurt J. Lesker, Innovate, Pittsburgh (2016).

40. S. M. Rossnagel and D. Mikalsen, "Collimated magnetron sputter deposition," *J. Vac. Sci. Technol. A* **9**, 261–265 (1990).

41. S. K. Dew et al., "Spatial and angular nonuniformities from collimated sputtering," *J. Vac. Sci. Technol. B* **11**, 1281–1286 (1993).

42. Z. Lin and T. S. Cale, "Flux distributions and deposition profiles from hexagonal collimators during sputter deposition," *J. Vac. Sci. Technol. A* **13**, 2183–2188 (1995).

43. D. M. Broadway, Y. Y. Platonov, and L. A. Gomez, "Achieving desired thickness gradients on flat and curved substrates," *Proc. SPIE* **3766**, 262–274 (1999).

44. K. Pfeiffer et al., "Antireflection coatings for strongly curved glass lenses by atomic layer deposition," *Coatings* **7**, 118–130 (2017).

45. T. M. Rodgers, H. Zhao, and H. N. G. Wadley, "Microstructure of vapor deposited coatings on curved substrates," *J. Vac. Sci. Technol. A,* **33**(5), 05E118 (2015).

46. S. Liedtke et al., "Crystalline Ti-nanostructures prepared by oblique angle deposition at room temperature," *J. Vac. Sci. Technol. B* **36**, 031804 (2018).

47. Z. Wang et al., "Angled physical vapor deposition techniques for non-conformal thin films and three-dimensional structures," *MRS Commun.* **6**, 17–22 (2016).

48. A. T. Lowe and C. D. Hosford, "Magnetron sputter coating of microspherical substrates," *J. Vac. Sci. Technol.* **16**, 197–199 (1979).

49. L. Zhang and X. Cai, "Uniform masks design method based on the shadow matrix for coatings materials with different condensation characteristics," *Sci. World.* **2013**, 160792 (2013).

50. C. Liu et al., "Theoretical design of shadowing masks for uniform coatings on spherical substrates in planetary rotation systems," *Opt. Express* **20**(21), 23790–23797 (2012).

51. F. Villa, A. Martinez, and L. E. Regalado, "Correction masks for thickness uniformity in large-area thin films," *Appl. Opt.* **39**, 1602–1610 (2000).

52. R. M. Tiggelaar et al., "Spreading of thin-film metal patterns deposited on nonplanar surfaces using a shadow mask micromachined in Si (110)," *J. Vac. Sci. Technol. B,* **25**, 1207–1216 (2007).

53. D. L. Windt and R. Conley, "Two dimensional differential deposition: figure correction of thin-shell mirror substrates for x-ray astronomy," *Proc. SPIE* **9603**, 96031H (2015).

54. K. Kilaru et al., "Improving x-ray optics via differential deposition," *Proc. SPIE* **10399**, 103991F (2017).

55. S. Trolier-McKinstry et al., "In situ annealing studies of sol-gel ferroelectric thin films by spectroscopic ellipsometry," *J. Am. Ceram. Soc.* **78**(7), 1907–1913 (1995).

56. H. Fujiwara, *Spectroscopic Ellipsometry Principles and Application*, Japanese ed., John Wiley and Sons, Ltd., Tokyo, Japan (2003).

57. G. E. Jellison, Jr. and F. A. Modine, "Parameterization of the optical functions of amorphous materials in the interband region," *Appl. Phys. Lett.* **69**, 371–373 (1996).

58. G. E. Jellison, Jr. et al., "Characterization of thin-film amorphous semiconductors using spectroscopic ellipsometry," *Thin Solid Films* **377**–**378**, 68–73 (2000).

59. G. E. Jellison, Jr., "Physics of optical metrology of silicon-based semiconductor devices," in A. C. Diebold, Ed., *Handbook of Silicon Semiconductor Metrology*, Marcel Dekker, Inc., New York, pp. 723–760 (2001).

60. D. V. Likhachev, N. Malkova, and L. Poslavsky, "Modified Tauc–Lorentz dispersion model leading to a more accurate representation of absorption features below the bandgap," *Thin solid Films* **589**, 844–851 (2015).

61. S. Yang, "Determination of the optical properties of sol–gel-derived Pb (ZrxTi1-x)O3 thin films by spectroscopic ellipsometry," *Ferroelectrics* **287**, 35–46 (2003).

62. C. H. Peng and S. B. Desu, "Structure development study of Pb(Zr, Ti)O3 thin films by an optical method," *J. Am. Ceram. Soc.* **77**(6), 1486–1492 (1994).

63. X. G. Tang et al., "Optical properties of Pb(ZrxTi1 − x)O3 (x = 0.4, 0.6) thin films on Pt-coated Si substrates studied by spectroscopic ellipsometry," *Mater. Chem. Phys.* **103**, 329–333 (2007).

64. A. Furuya and S. Hirono, "Target magnetic-field effects on deposition rate in RF magnetron sputtering," *J. Appl. Phys.* **68**, 304–310 (1990).

65. T. Kobayashi et al., "Method for simulating the thickness distribution of a cubic boron nitride film deposited on a curved substrate using ion-beam-assisted vapor deposition," *Phys. Procedia* **32**, 831–839 (2012).

66. Q. Fan, "Uniformity of targets erosion and magnetic film thickness distribution in the target-facing-type sputtering method," *J. Vac. Sci. Technol. A* **10**, 3371–3375 (1992).

67. N. D. Madsen et al., "Controlling the deposition rate during target erosion in reactive pulsed DC magnetron sputter deposition of alumina," *Surf. Coat. Technol.* **206**, 4850–4854 (2012).

68. P. G. Quigley, R. A. Rao, and C. B. Eom, "Time dependence and spatial distribution of the deposition rate of $YBa_2Cu_3O_7$ thin films in 90° off-axis sputtering," *J. Vac. Sci. Technol. A* **15**, 2854–2858 (1997).

69. L. Raimondi and D. Spiga, "Mirrors for x-ray telescopes: Fresnel diffraction-based computation of point spread functions from metrology," *Astron. Astrophys.* **573**, A22 (2015).

70. D. D. M. Ferreira et al., "Design, development, and performance of X-ray mirror coatings for the ATHENA mission," *Proc. SPIE* **10399**, 1039918 (2017).

71. A. Brewer et al., "Uniform sputter deposition of high-quality epitaxial complex oxide thin films," *J. Vac. Sci. Technol. A* **35**, 060607 (2017).

72. V. Vyas and M. J. Kushner, "Scaling of hollow cathode magnetrons for ionized metal physical vapor deposition," *J. Vac. Sci. Technol. A* **24**, 1955–1969 (2006).

73. G. Brauer et al., "Magnetron sputtering–milestones of 30 years," *Vacuum* **84**, 1354–1359 (2010).

74. J. S. Bessey and J. A. Roth, "Sputtered iridium coatings for grazing incidence x-ray reflectance," *Proc. SPIE* **2011**, 12–17 (1994).

75. Y. Yao et al., "Stress manipulated coating for fabricating lightweight X-ray telescope mirrors," *Opt. Express* **23**(22), 28605–18 (2015).

76. Y. Yao et al., "Thermal oxide patterning method for compensating coating stress in silicon x/ray telescope mirrors," *Proc. SPIE* **10699**, 1069942 (2018).

Biographies of the authors are not available.